RESEARCH ARTICLE

Optimal Path Planning Method for IMU System-Level Calibration Based on Improved Dijkstra's Algorithm

XUESONG BAI, LU WANG [ID], YUANBIAO HU, PINGFEI LI, AND YUTONG ZU

Key Laboratory of Deep Geo-Drilling Technology, Ministry of Natural Resources, Beijing 100083, China
School of Engineering and Technology, China University of Geosciences, Beijing 100083, China

Corresponding author: Lu Wang (wanglu666@cugb.edu.cn)

ABSTRACT The calibration path of system-level calibration directly affects the incentive effect of the error term and thus the calibration accuracy. Currently, the planning of system-level calibration paths is predominantly designed based on personal experience, resulting in insufficient incentive for error terms, low calibration accuracy, and long calibration times. Therefore, this study proposes a system-level calibration optimal path planning method based on an improved Dijkstra's algorithm. First, the system-level calibration optimal path planning problem was modeled as a multi-fork regular root tree model, and the adaptability of Dijkstra's algorithm was improved. Second, a 30-dimensional Kalman filter model was designed for system-level calibration. Then, simulation experiments were conducted, and the results demonstrated that the calibration accuracy of the error term reached 90% within 330 s. Finally, a Micro-Electro-Mechanical system (MEMS) inertial sensor, model PA-IMU488B, was used for experimental verification, and the results were compared with the discrete calibration results. The results indicate that the bias and scale factor errors of the MEMS inertial sensor reached the target accuracy within 5 min. The optimal path planning method for system-level calibration proposed in this study is not dependent on a high-precision turntable, is applicable to sensors of different accuracies, and decreases calibration time while ensuring calibration accuracy.

INDEX TERMS Calibration algorithm, system-level calibration, Dijkstra's algorithm.

I. INTRODUCTION

The navigation accuracy of the strap-down inertial navigation system (SINS) depends on the measurement accuracy of the inertial measurement unit (IMU) [1]. To achieve high accuracy navigation, the IMU must be calibrated before use [2].

For the calibration method of SINS, previous researchers have done a lot of work. Their contribution mainly can be divided into discrete calibration method and system level calibration method [3]. The discrete calibration is to observe the output data according to the exact input datum, and then determine the error parameters by the least square fitting method. Generally including angular rate calibration experiment and static position experiment [4], [5]. Discrete calibration is a direct measurement method, which requires the

turntable to provide accurate input as a reference. Therefore, the calibration accuracy largely depends on the precision of the turntable. In addition, it is time-consuming and only suitable for laboratory conditions. The system level calibration method introduces the IMU error into the navigation error of the navigation solution. Then, the parameters of the inertial error model can be identified by taking the navigation calculation results as observations [6]. The system level calibration can achieve high calibration accuracy by using low precision test tools and reduce the accuracy requirements of calibration test tools. At the same time, there is no need to measure and record the output of gyroscope or accelerometer, which is convenient for engineering application. The key to system-level calibration is to establish the relationship between navigation error and sensor error and to fully motivate the sensor error through a reasonable calibration path arrangement. Therefore, the design of calibration path will

The associate editor coordinating the review of this manuscript and approving it for publication was Halil Ersin Soken [ID].

directly affect the accuracy of system level calibration results. The unreasonable calibration path not only wastes time but also makes the error parameter estimation wrong.

In recent years, scholars have proposed many system-level calibration methods, which can be generally divided into multi-position fitting method and Kalman filtering based method [7]. Fitting calibration method, which is based on the SINS error equation, fits the parameters of the inertial calibration model by the least square method. Many improvements have been proposed from the perspective of calibration path, error models and iterative algorithms [8], [9], [10], [11]. This calibration method can be realized by low precision turntable. But the improvement of its accuracy requires the use of complex iterative algorithms and cumbersome operation. The application of Kalman filter in calibration parameter estimation can be traced to the work of Hellings and Kitzerow in the 1970s [7]. Kalman filter calibration method can get rid of the influence of turntable precision on calibration results. At present, the research of this method mainly focuses on the design of Kalman filter and the arrangement of calibration path. Aiming at the complex error characteristics of IMU, some researchers have established different error models and used Kalman filters with different dimensions to estimate them [12], [13], [14], [15], [16]. Wang et al. [17] regarded navigation error as observable error and proposed using extended Kalman filter to estimate error parameters. Glueck et al. [18] proposed an auto calibration scheme to estimate the error parameters of an accelerometer using unscented Kalman filter (UKF). Further, Cheng et al. [19] proposed a high-precision calibration scheme for redundant inertial measurement, and compared the results of the Kalman filter (KF), extended Kalman filter (EKF), and unscented Kalman filter (UKF). Xu et al. [20] proposed a hybrid calibration method for FOG-based IMU, combination method of coarse and accurate calibration. The calibration path planning needs to decouple the errors and make the error parameters observable. Camberlein et al. [21] designed an 18-position calibration path, which could calibrate the laser gyro within 20 min and meet the accuracy requirements of the navigation level accuracy. Wang et al. [22] proposed a 19-position scheme calibration method for fiber optic gyroscope SINS based on observability analysis and considered the effect of gravity anomalies. Wang et al. [23] proposed a 36-state EKF for the Fiber-optic gyroscope SINS, based on 24-position, and an iterative calibration method has been suggested to suppress calibration residuals. Cai et al. [24] proposed a 51-state filter for 18 rotations, and its five-day inertial navigation results position accuracy can be improved by approximately 8%.

In summary, the system-level calibration method based on Kalman filter is a suitable calibration method for IMU with different precision, and this method can be used without the turntable. However, in the above studies, less attention is paid to the optimization design of calibration path, which is mostly based on the personal experience of researchers. After the path design is completed, the observability degree analysis based on singular value decomposition is generally used to verify the path design. However, the influence of calibration path on calibration time and accuracy was not analyzed. Moreover, the calibration path may not be applicable when the calibration conditions change, and it needs to be redesigned and analyzed. This limits the generalization of system-level calibration in applications. Therefore, it is necessary to propose an optimal calibration path planning method, which can effectively carry out system-level calibration path planning according to different usage scenarios. At the same time, the optimization of calibration path is beneficial to improve the accuracy of error estimation, shorten the calibration time and simplify the calibration operation.

This study proposes a system level calibration path planning method based on improved Dijkstra's algorithm. The method adopts the observability analysis method based on the mean square error matrix, and the calibration path can be planned quantitatively according to the convergence of each error. At the same time, the prediction of residual error variance can be obtained, that is, different calibration target accuracies can be preset. By changing the Kalman filter model (state quantity, system noise, etc.) in the proposed path planning algorithm, the calibration path planning under different calibration requirements and calibration scenarios can be realized. This method plans calibration path according to actual calibration conditions, which is of great significance to improve the precision of high-precision IMU system-level calibration, calibration efficiency of large batch IMU and in-field calibration without a turntable.

The paper is organized as follows. Section II describes the optimal path design method based on the improved Dijkstra's algorithm. Section III demonstrates the accuracy and effectiveness of the method through simulation experiments. In Section IV, the accuracy of the method is verified using experiments. The application of this method is discussed in Section V. The conclusions are drawn in Section VI.

II. THEORY AND METHOD
A. IMPROVED DIJKSTRA'S ALGORITHM SUITABLE FOR CALIBRATED PATH PLANNING

The traditional Dijkstra's algorithm is a breadth-first search for solving single-source shortest path problems with weighted directed graphs [25]. The basic concept is to use the greedy algorithm to expand the nearest node from the starting point, and then update the distance between it and its neighbors until the end point. This requires that the weights of each edge in the graph be positive. This algorithm has been applied in different fields, and many researchers have made adaptive improvements to its use [26], [27], [28], [29], [30]. Because the purpose of optimal calibration path planning is not to find the shortest distance between two points in the known graph, the location of the target node is uncertain. The judgment condition changed from "shortest path" to "maximum weight". The distance between nodes in the graph used by the traditional algorithm is known and fixed and does not change with the change of the path. In the problem

in this paper, the path has after-effect, that is, the past path will affect the weight of the future path edge. Therefore, the traditional Dijkstra's algorithm cannot be directly applied to the case in this paper. This study improves the traditional Dijkstra's algorithm accordingly. In the improved algorithm, path expansion is only carried out near the new node. Each node update means that the number of rotations increases or a better rotation scheme is found. In addition, the end condition of improved Dijkstra's algorithm is that the observability degree of the current path reaches the target value, or the length of the current path exceeds the set maximum value. To solve this problem, this paper proposes to take the observability degree as the weight and the maximum value of the weight sum as the objective function. This can ensure that the obtained calibration path can fully realize the estimation of the error parameters.

The system-level calibration process generally ensures that the IMU rotates in place. The same attitude of the IMU may appear several times in the calibration path, but the calibration effect achieved at each occurrence is not the same, that is, the calibration effect of the attitude is influenced by the previous calibration process. Therefore, this study proposes an improved Dijkstra's algorithm that considers the system-level calibrated path planning problem as a multi-fork regular root tree G. As shown in Fig. 1, model G is simple, of low calculation, and applicable to system-level calibrated optimal path planning.

The multi-fork regular root tree G is expressed as follows:

$$G = (V, E, W) \quad (1)$$

where V is the set of nodes in G, $V = \{v_1, v_2, \cdots, v_n\}$, element v_i indicates the attitude that reach after the IMU rotational movement in the calibration path, $n = m \times r + 1$ represents the number of possible attitudes in the calibration path, m represents the number of rotation modes, and r represents the number of rotations.

E is the set of edges in G, $E = \{e_1, e_2, \cdots, e_{n-1}\}$, $e_i = [v_i, v_j]$, and e_i represents the movement of the IMU from attitude v_i to attitude v_j.

W is the set of weights of the corresponding edges, $W = \{w_1, w_2, \cdots, w_{n-1}\}$, $w_i(e_i) = w([v_i, v_j])$, where $w_i(e_i)$ represents the sum of the observability degree increments during the process of the IMU from attitude v_i to attitude v_j. The weight w represents the increment of observability degree in this rotation, and the increase of observability degree represents the decrease of residual error. Therefore, the estimation effect of error state quantity can be quantitatively characterized. The higher the weight is, the more the rotation increases the total observability degree. In this way, the current best rotation scheme can be selected, that is, the error can be better motivated and the result can be estimated. As shown in (2). the greater the increment in observability degree and the greater the weight, the better the calibration effect of the moving
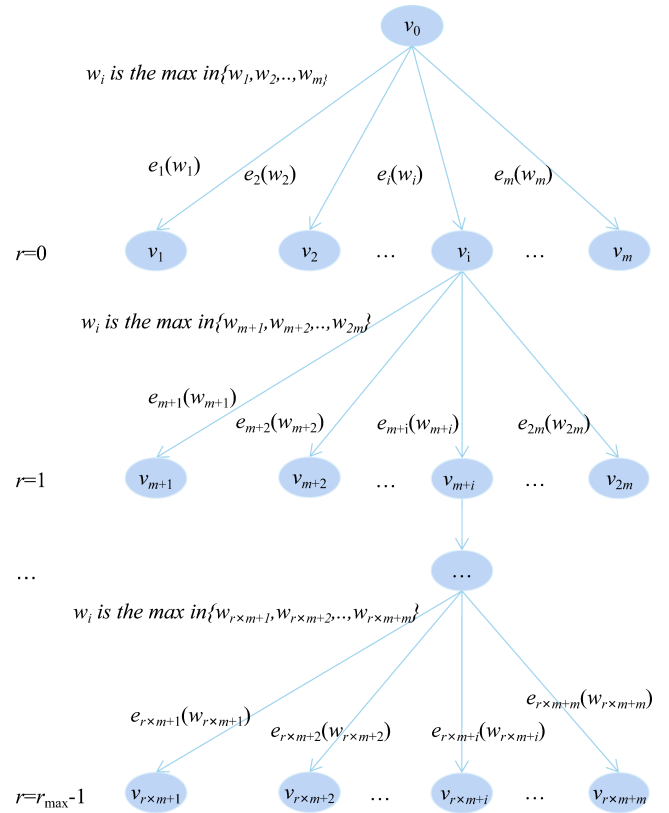

FIGURE 1. Multi-fork regular root tree model for calibration path planning.

process e_i.

$$w_i(e_i) = \sum_{p=1}^{q} \max[\sigma_{v_i(p)}, \sigma_{\max}] - \sum_{p=1}^{q} \max[\sigma_{v_j(p)}, \sigma_{\max}], \quad (2)$$

where $\sigma_{v_i(p)}$ and $\sigma_{v_j(p)}$ represent the observability degree corresponding to the pth error term of the IMU under the attitudes v_i and v_j, and q is the total number of error terms required to be calibrated in the system-level calibration. $\sigma_{\max}$ is the target calibration accuracy, representing the expected observability degree of an error term in the method used in this study. The calibration of the error term is terminated when the observability degree of the error term has reached the target calibration accuracy, $\sigma_{\max}$, during the system level calibration. $\sigma_{v_i(p)}$ is the observability degree of the pth error term, v_i [31], as shown in (3):

$$\sigma_{v_i(p)} = \sqrt{\frac{P_{0(pp)}}{P_{v_i(pp)}}}, \quad (3)$$

where P_0 is the covariance matrix of Kalman filter at the initial time, P_{v_i} is the covariance matrix of Kalman filter in v_i attitude, the subscript pp represents the entries in row p column p of the matrix.

In the optimal calibration path designed in this study, the IMU was rotated forward and backward around the X-, Y-, and Z-axes of the IMU in six rotational motions, namely
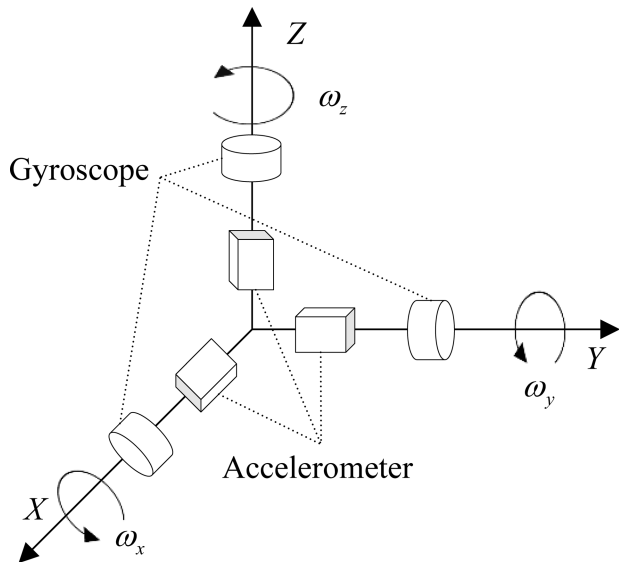
FIGURE 2. The diagram of turntable rotation.

FIGURE 3. Flow chart of optimal path planning algorithm.

$m = 6$. Moreover, the speed and angle of each rotation are set to a fixed value to ensure that the weights $w([v_i, v_j])$ are only related to the rotation mode during the path planning process. Simulation diagram of turntable rotation is shown in Fig. 2.

The optimal path planning process based on the improved Dijkstra's algorithm is as follows, as shown in Fig. 3.

1) First, initialize the variable. It includes the maximum number of rotations r_{max}, number of rotations r = 0, target observability degree σ_{max}, initial attitude v_0, number of error terms to be calibrated q, an array R for storing the paths, and an array O for storing the weights.

2) In the second step, six different rotations are performed starting from the attitude v_0, and six different attitudes $v_{r \times m+1}$ to $v_{r \times m+6}$ can be reached. Based on the set error values, the IMU data with errors corresponding to the six rotations are obtained via simulations, and their observability degree increments w are calculated separately.

3) The third step is comparing the magnitude of $w_{r \times m+1}$ to $w_{r \times m+6}$. If $w_{r \times m+a}$ is the maximum, $v_{r \times m+a}$ is considered as the next attitude in the optimal calibration path and deposited in the array R. $w_{r \times m+a}$ is the sum of the observability degree increments for this rotation deposited in the array O, and $e_{r \times m+a}$ is the current action in the optimal calibration path.

4) In the fourth step, it is determined if the observability degree reaches the target value and if the maximum number of rotations has been reached.

5) Finally, starting from the attitude $v_{r \times m+a}$, steps 2-4 are repeated until the path length exceeds the set value or the observability degree reaches the desired value, and the obtained R is the optimal calibration path.
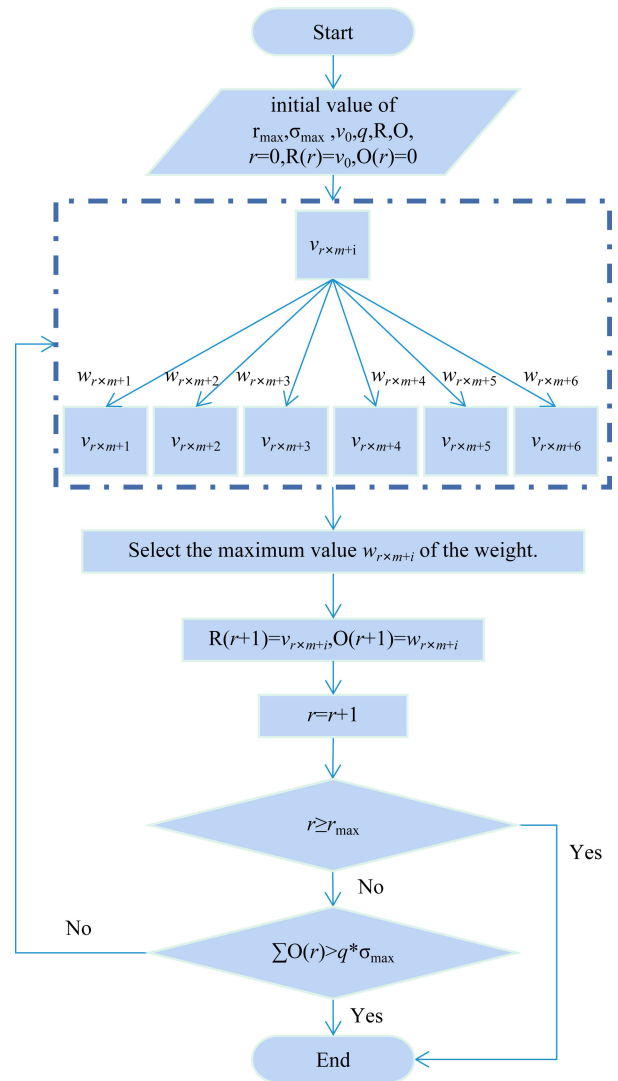
B. SYSTEM-LEVEL CALIBRATION KALMAN FILTERING MODEL

The IMU comprises three gyroscopes and three accelerometers. Considering the bias error, non-orthogonal error, and scale factor error of the three-axis gyroscopes and three-axis accelerometers, the error model [32] is established as follows:

$$\begin{bmatrix} \delta f_x^b \\ \delta f_y^b \\ \delta f_z^b \end{bmatrix} = \begin{bmatrix} \delta K_{axx} & 0 & 0 \\ \delta K_{ayx} & \delta K_{ayy} & 0 \\ \delta K_{azx} & \delta K_{azy} & \delta K_{azz} \end{bmatrix} \begin{bmatrix} f_x^b \\ f_y^b \\ f_z^b \end{bmatrix} + \begin{bmatrix} B_{ax} \\ B_{ay} \\ B_{az} \end{bmatrix}, \quad (4)$$

where δf_i^b ($i = x, y, z$) represents the measurement error of the i axis accelerometer, f_i^b represents the ideal value of the i axis accelerometer, B_{ai} represents the bias of the i axis accelerometer, δK_{aii} represents the scale factor error of the i axis accelerometer, δK_{aij} ($i \neq j, j = x, y, z$) represents the non-orthogonal error of i axis relative to j axis accelerometer.

Similarly, the error model of the gyroscope was developed in the b-system as:

$$
\begin{bmatrix} \delta\omega_x^b \\ \delta\omega_y^b \\ \delta\omega_z^b \end{bmatrix} = \begin{bmatrix} \delta K_{gxx} & \delta K_{gxy} & \delta K_{gxz} \\ \delta K_{gyx} & \delta K_{gyy} & \delta K_{gyz} \\ \delta K_{gzx} & \delta K_{gzy} & \delta K_{gzz} \end{bmatrix} \begin{bmatrix} \omega_x^b \\ \omega_y^b \\ \omega_z^b \end{bmatrix} + \begin{bmatrix} B_{gx} \\ B_{gy} \\ B_{gz} \end{bmatrix}, \quad (5)
$$

where $\delta\omega_i^b$ ($i = x, y, z$) represents the measurement error of the i axis gyroscope, ω_i^b represents the ideal value of the i axis gyroscope, B_{gi} represents the bias of the i axis gyroscope, δK_{gii} represents the scale factor error of the i axis gyroscope, δK_{gij} ($i \neq j, j = x, y, z$) represents the non-orthogonal error of i axis relative to j axis gyroscope.

As shown in (4) and (5), the inertial instrument error model established in this study includes a total of 21 error terms, of which 9 are accelerometer errors and 12 are gyroscope errors, and the parameters are no longer coupled to each other, and the calibration results are unique [33].

To identify errors, such as bias, scale factor, and non-orthogonal error of gyroscopes and accelerometers, a 30-dimensional Kalman filter model [34] was designed as shown in the following equation:

$$
\begin{cases} \dot{X} = FX + GW \\ Z = HX + V \end{cases}, \quad (6)
$$

where X is the 30-dimensional state vector, Z is the 6-dimensional measurement vector, F is the state transfer matrix, G is the system noise distribution matrix, H is the measurement matrix, W is the 6-dimensional system noise vector, and V is the 6-dimensional measurement noise vector.

Of which,

$$
X = \begin{bmatrix} \varphi_E & \varphi_N & \varphi_U & \delta v_E & \delta v_N & \delta v_U \\ \delta L & \delta\lambda & \delta h & B_{gx} & B_{gy} & B_{gz} \\ B_{ax} & B_{ay} & B_{az} & \delta K_{gxx} & \delta K_{gyx} & \delta K_{gzx} \\ \delta K_{gxy} & \delta K_{gyy} & \delta K_{gyz} & \delta K_{gxz} & \delta K_{gyz} & \delta K_{gzz} \\ \delta K_{axx} & \delta K_{ayx} & \delta K_{azx} & \delta K_{ayy} & \delta K_{azy} & \delta K_{azz} \end{bmatrix},
$$

$$
Z = \begin{bmatrix} \delta v_E & \delta v_N & \delta v_U & \delta L & \delta\lambda & \delta h \end{bmatrix},
$$

$$
H = \begin{bmatrix} 0_{3\times3} & I_{3\times3} & 0_{3\times3} & 0_{3\times21} \\ 0_{3\times3} & 0_{3\times3} & I_{3\times3} & 0_{3\times21} \end{bmatrix}, \quad G = \begin{bmatrix} -C_b^n & 0_{3\times3} \\ 0_{3\times3} & C_b^n \\ 0_{24\times3} & 0_{24\times3} \end{bmatrix},
$$

$$
W = \begin{bmatrix} \omega_{g3\times1} \\ \omega_{a3\times1} \end{bmatrix}, \quad V = \begin{bmatrix} V_{v3\times1} \\ V_{p3\times1} \end{bmatrix}, \quad (7)
$$

where $\varphi = \begin{bmatrix} \varphi_E & \varphi_N & \varphi_U \end{bmatrix}^T$ are the misalignment angles between n frame and n' frame; $\delta v = \begin{bmatrix} \delta v_E & \delta v_N & \delta v_U \end{bmatrix}^T$ are the velocity errors in n frame; $\delta p = \begin{bmatrix} \delta L & \delta\lambda & \delta h \end{bmatrix}$ are the latitude error, the longitude error, and the height error, respectively. The state transfer matrix F is derived from the sensor error model and the SINS error equation [35]. $I_{3\times3}$ is the unit matrix, C_b^n is the SINS attitude matrix, $\omega_{g3\times1}$ is gyroscope noise, $\omega_{a3\times1}$ is accelerometer noise, $V_{v3\times1}$ is
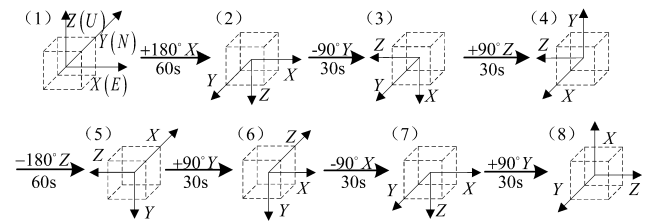

FIGURE 4. Rotation Scheme.

velocity observation noise, and $V_{p3\times1}$ is position observation noise.

III. SIMULATION EXPERIMENTS

A. SIMULATION CONDITIONS SETTING

The correctness of the proposed method is verified by numerical simulation with MATLAB. The IMU error term and Kalman filter parameters were set. The performance index of the MEMS-IMU simulation data is shown in Table 1 [36]. The angular random walk of the gyroscope is $0.25° / \sqrt{h}$ and the velocity random walk of the accelerometer is 100 $\mu g / \sqrt{Hz}$. The initial attitude error was set as $\begin{bmatrix} 5' & 5' & 5' \end{bmatrix}$, observation noise at zero velocity was $V_{v3\times1} = \begin{bmatrix} 0.01 & 0.01 & 0.01 \end{bmatrix}^T$ m/s, and position observation noise was $V_{p3\times1} = \begin{bmatrix} 0.01 & 0.01 & 0.01 \end{bmatrix}^T$ m. The sensor sampling frequency was 100 Hz and the target observability degree was selected as $\sigma_{max} = 10$.

The larger the input rotation rate is, the larger the error of the system parameters will be. If the input angular rate is too small, the observability degree of the scale factor error and non-orthogonal error of the gyro will be small. However, if the input angular rate is too large, the gyro deviation will be submerged in the observation noise, and the estimation result cannot be effectively determined. In this paper, the angular rate input is 3 °/s.

B. SIMULATION EXAMPLES

First, according to the above simulation conditions, simulation data of six rotations of the IMU around the X, Y and Z axes were generated. The observability degree was calculated by Kalman filter. Then, we compared and selected the scheme with the highest observability degree as the rotation mode of this step. Finally, the above steps were repeated until the observability degree reached the target value 10.

The calibration rotation scheme obtained using the calibration path planning algorithm proposed in this study is shown in Fig. 4. The IMU was stationary for 60 s at the beginning and final positions respectively. The calibration took 390 s after a total of 8 positions.

The error terms of the IMU were calibrated using the system-level calibrated Kalman filter model discussed in Section .II B. The observability degree of each error term is shown in Fig. 5-6. The estimation results of each error term are shown in Fig. 7-8.
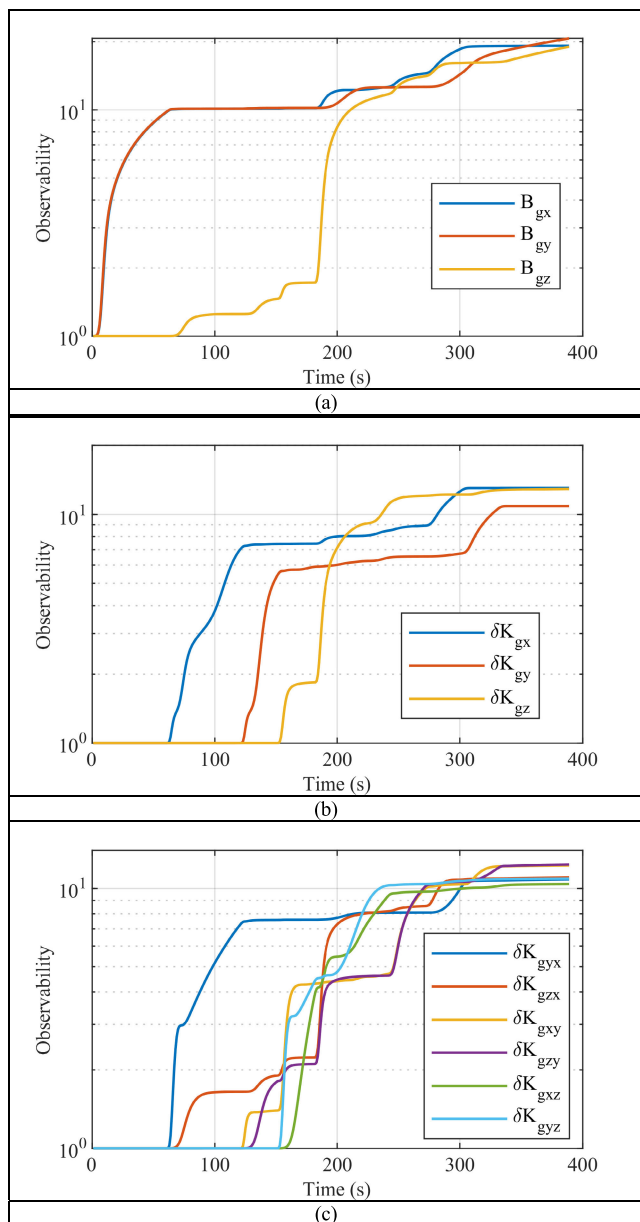
FIGURE 5. Simulation results of optimal calibration path (a) Gyro bias error, (b) Gyro scale factor error, (c) Gyro non-orthogonal error.

FIGURE 6. Simulation observability degree of optimal calibration path (a) Accelerometer bias error, (b) Accelerometer scale factor error, (c) Accelerometer non-orthogonal error.

Fig. 5 showed the observability degree of gyro error terms in the optimal calibration path. In Fig. 5(a) from 0 s to 60 s, the observability of B_{gx} and B_{gy} increased while B_{gz} didn't. From 60 s to 240 s, the observability degree of B_{gz} began to increase. After 240s, the observability of B_{gx}, B_{gy}, and B_{gz} all reached to the target value 10. In Fig. 5(b), the observability degree of δK_{gx}, δK_{gy}, δK_{gz} increased at 60 s, 120 s and 150 s respectively. It is consistent with the rotation sequence showed in Fig. 4 that the IMU rotates around X axis, Y axis and Z axis at 60 s, 120 s and 150 s respectively. In Fig. 5(c), each non - orthogonal error was motivated when the corresponding axis rotated, which made the observability degree increase continuously. Fig. 5 declared that by the
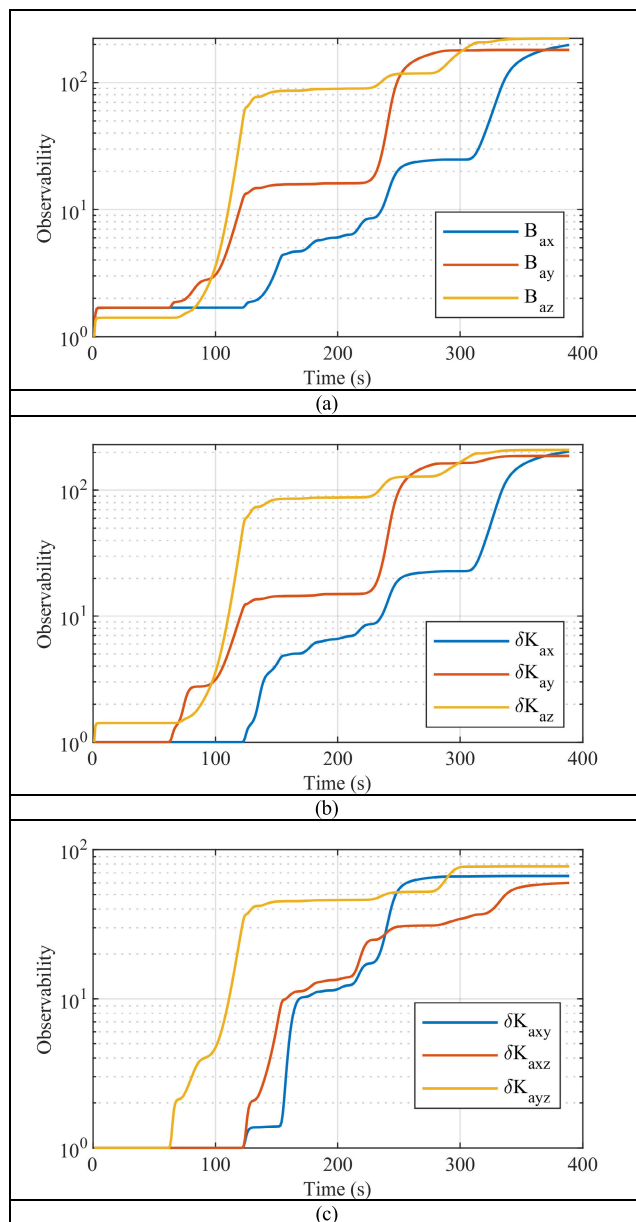
optimal calibration path, the observability degree of all the gyro error terms reached to the target value.

Fig. 6 showed the observability degree of accelerometer error terms in the optimal calibration path. In Fig. 6(a) from 0 to 60 s, the observability of B_{ax}, B_{ay} and B_{az} increased while B_{az} was slightly lower. At 60 s, the observability degree of B_{ay} and B_{az} began to increase rapidly. And the observability degree of B_{ax} increased continuously from 120 s. After 240 s, the observability of B_{ax}, B_{ay} and B_{az} all reached to the target value 10. In Fig. 6(b), the observability degree of δK_{ax}, δK_{ay}, δK_{az} increased at 0 s, 60 s and 120 s respectively. At these moments, their corresponding accelerometers were affected by gravity, which is consistent with the rotation
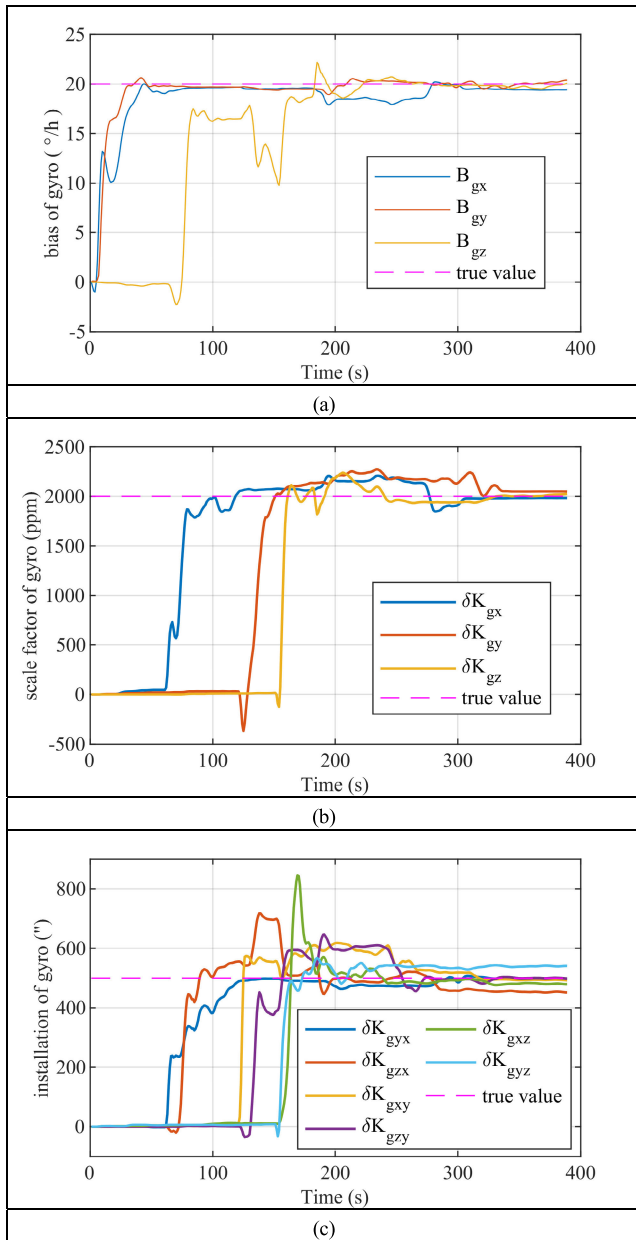
FIGURE 7. Simulation results of optimal calibration path (a) Gyro bias error, (b) Gyro scale factor error, (c) Gyro non-orthogonal error.

FIGURE 8. Simulation results of optimal calibration path (a) Accelerometer bias error, (b) Accelerometer scale factor error, (c) Accelerometer non-orthogonal error.

sequence showed in Fig. 4. In Fig. 6(c), each non - orthogonal error was motivated when the corresponding axis deviated from the horizontal direction, which made the observability degree increase continuously. Fig. 6 declared that by the optimal calibration path, the observability degree of all the accelerometer error terms also reached to a high value.

Fig. 7 showed the simulation results of gyroscope system-level calibration. From 0 s to 60 s, the estimated curves of B_{gx} and B_{gy} in Fig. 7(a) increased while others didn't. At 60 s, 120 s, 150 s, the other error terms were motivated respectively and rapidly converge to the true value. After 330 s, the IMU was stationary, all the error terms reached convergence.
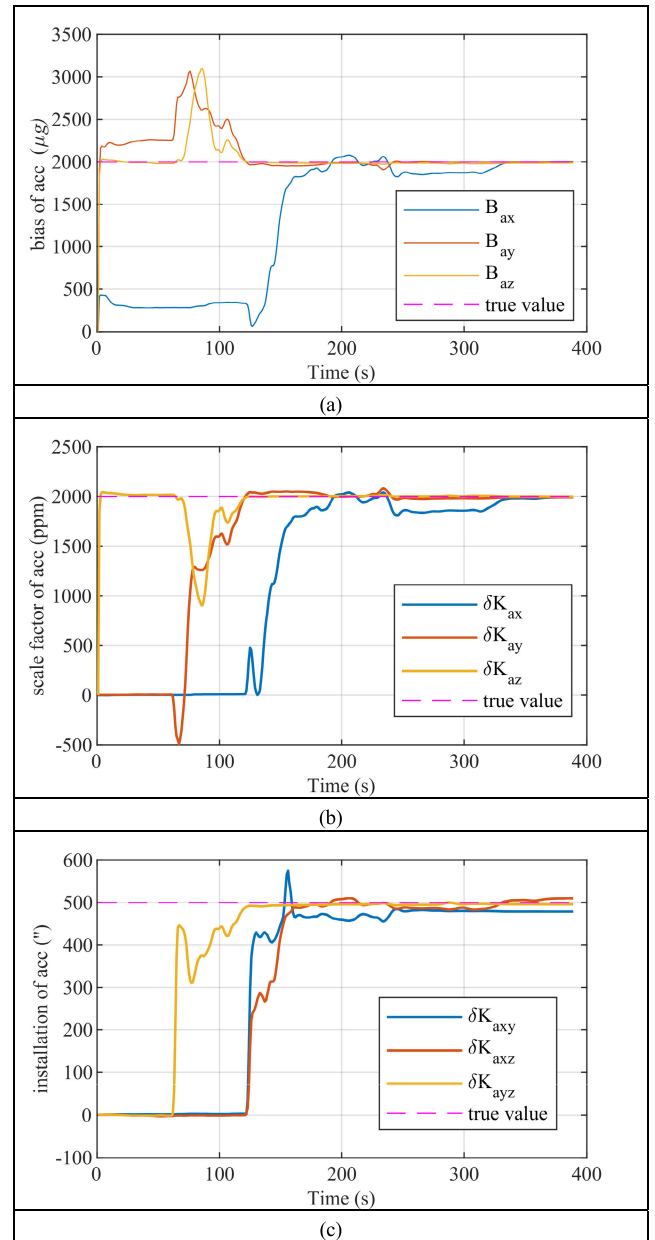
Fig. 8 showed the simulation results of accelerometer system-level calibration. From 0 s to 60 s, B_{ay}, B_{az}, δK_{az} were well estimated. At 60 s, 120 s, 150 s, the other error terms were motivated respectively and rapidly converged to the true value. It can also be found that the B_{ay}, B_{az} suddenly increased and exceeded the real value. This is because the scaling factor and the non-orthogonal error of the corresponding axis were motivated, resulting in the wrong estimation of the bias. Under the action of Kalman filter, the error estimation gradually converged to the correct value. In the process of rotating motion, the error terms behavior basically conformed to the result of observability degree analysis. And
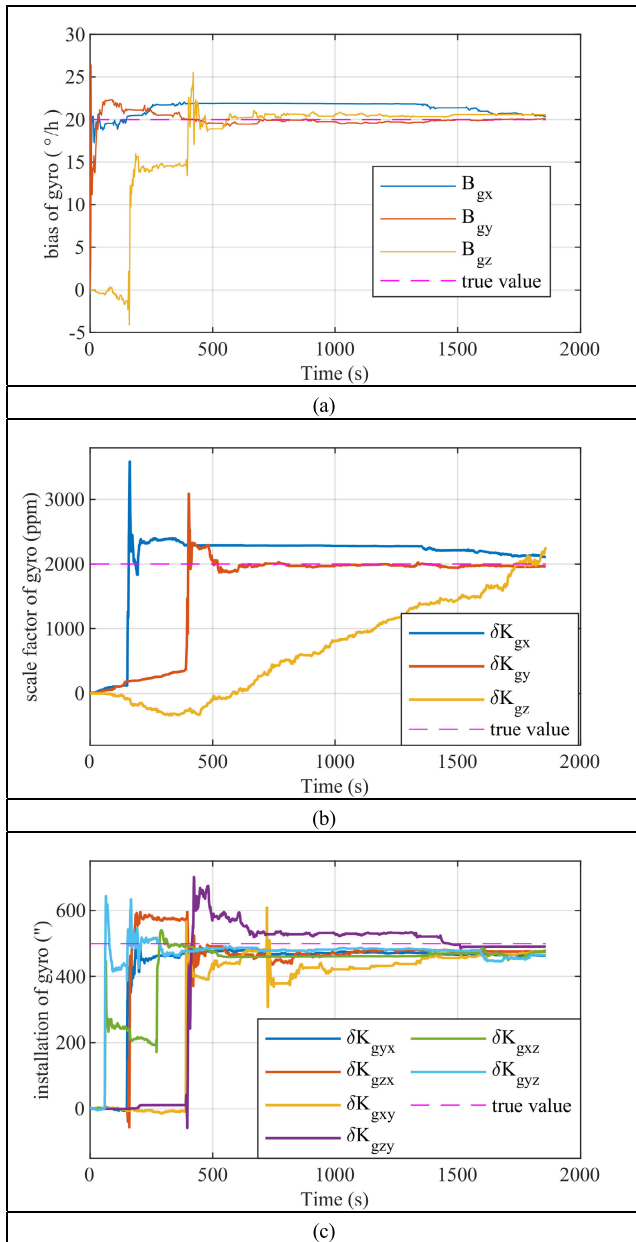
FIGURE 9. Simulation results of 18-position calibration path (a) Gyro bias error, (b) Gyro scale factor error, (c) Gyro non-orthogonal error.

FIGURE 10. Simulation results of 18-position calibration path (a) Accelerometer bias error, (b) Accelerometer scale factor error, (c) Accelerometer non-orthogonal error.

TABLE 1. IMU error terms for simulation.

Error terms	Error values
gyro constant bias (°/h)	20
acc constant bias (mg)	2
gyro scale factor error (ppm)	2000
acc scale factor error (ppm)	2000
gyro non-orthogonal error (″)	500
acc non-orthogonal error (″)	500

the error terms with strong observability degree converged faster. Because of the interference of noise, the error parameters fluctuate slightly in the convergence process. But in the last 60 s, they all converged to the real value.

In order to verify the superiority of the calibration path planned in this paper, the commonly used 18-position calibration path was used for simulation comparison under the same calibration conditions [20]. And the results were shown in Fig. 9 and Fig. 10, the total time of this method was 1860 s. Simulation results showed that most of the errors of the traditional scheme can be estimated, but the scaling factor of the Z-axis gyroscope cannot converge.
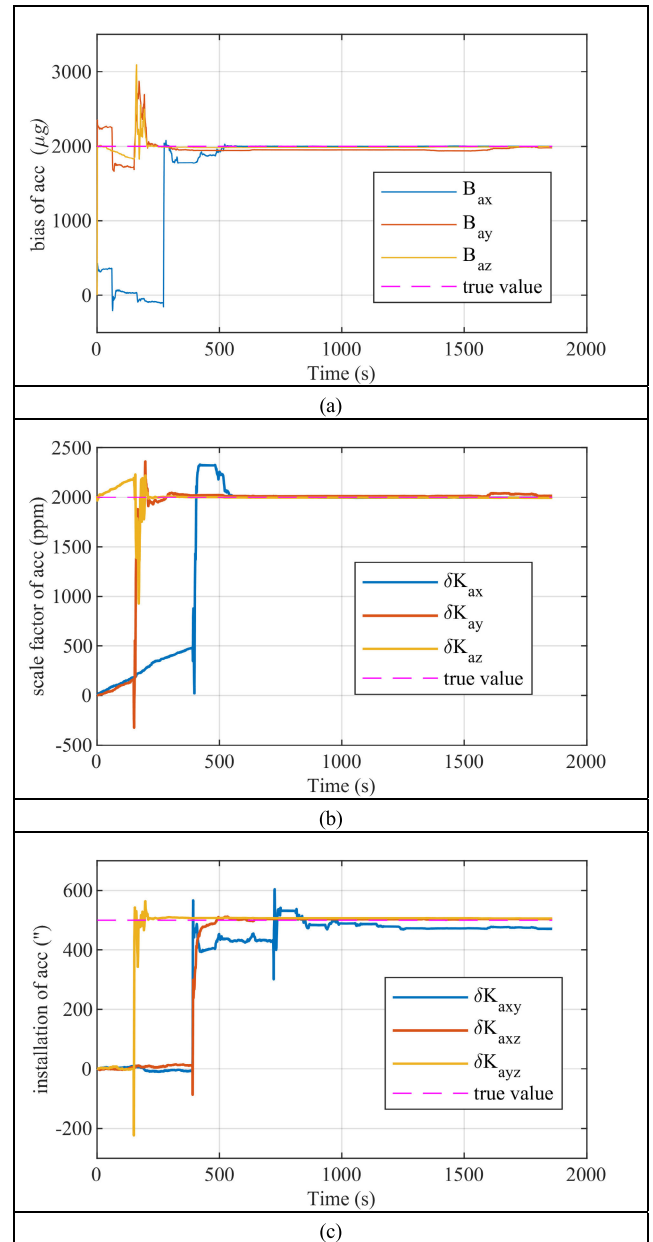
The calibration estimation results of each error and their relative errors were shown in Table 2. It can be seen from Table 2 that the estimation effects of the two schemes on

TABLE 2. Comparison of calibration results between optimal scheme and 18 position scheme.

Error coefficients	True value	Optimal scheme		18-position scheme	
		Estimate values	Relative error	Estimate values	Relative error
B_{gx} (°/h)	20	19.42	-2.9%	20.40	2.00%
B_{gy} (°/h)	20	20.38	1.9%	20.17	0.85%
B_{gz} (°/h)	20	20.07	0.35%	20.59	2.95%
δK_{gx} (ppm)	2000	1982.84	-0.86%	2106.79	5.34%
δK_{gy} (ppm)	2000	2050.19	2.51%	1960.15	-1.99%
δK_{gz} (ppm)	2000	2025.60	1.28%	2230.29	11.51%
δK_{gyx} (″)	500	496.34	-0.73%	462.60	-7.78%
δK_{gzx} (″)	500	451.87	-9.62%	475.52	-4.90%
δK_{gxy} (″)	500	492.91	-1.42%	478.67	-4.27%
δK_{gzy} (″)	500	498.54	-0.29%	491.25	-1.75%
δK_{gxz} (″)	500	479.72	-4.06%	477.74	-4.45%
δK_{gyz} (″)	500	540.91	8.18%	464.71	-7.06%
B_{ax} (μg)	2000	2004.56	0.23%	2000.5	0.03%
B_{ay} (μg)	2000	2001.65	0.08%	1976.96	-1.15%
B_{az} (μg)	2000	1988.02	-0.60%	1996.80	-0.16%
δK_{ax} (ppm)	2000	1993.48	-0.33%	1996.95	-0.15%
δK_{ay} (ppm)	2000	1993.78	-0.31%	2015.19	0.76%
δK_{az} (ppm)	2000	2000.33	0.02%	1994.15	-0.29%
δK_{ayx} (″)	500	479.08	-4.18%	470.95	-5.81%
δK_{azx} (″)	500	509.91	1.98%	503.99	0.80%
δK_{azy} (″)	500	496.19	-0.76%	505.78	1.16%
Total calibration time		390s		1860s	

FIGURE 11. Rotation scheme.

FIGURE 12. MEMS-IMU PA-IMU488B and calibration test with hands.

accelerometer error parameters are basically similar. But for the gyroscope scaling factor, the relative error of the estimated value obtained by the proposed method was significantly smaller than that of the traditional scheme. The calibration results of gyroscope obtained by the two schemes were worse than the calibration results of accelerometer. This also accords with the result of observability degree analysis: the observability degree of each error parameter of accelerometer was much higher than that of gyroscope. This was due to the small rotation rate of the input and hence insufficient excitation of the gyroscope scaling factor and non-orthogonal errors.

Through the comparison of simulation results, it can be clearly seen that under the current calibration conditions, the calibration path planned in this paper takes less time, has fewer rotations, and has better calibration effect. After changing the calibration conditions, the traditional scheme cannot even achieve the convergence of all error parameters, which proves the necessity of optimal calibration path design.

IV. EXPERIMENTAL VERIFICATION

To experimentally verify the performance of the algorithm, MEMS-IMU, model PA-IMU488B. The bias instability of the gyroscope was 2 °/h (Allan's variance), and the bias instability of the accelerometer was 0.1 mg. First, the sensor
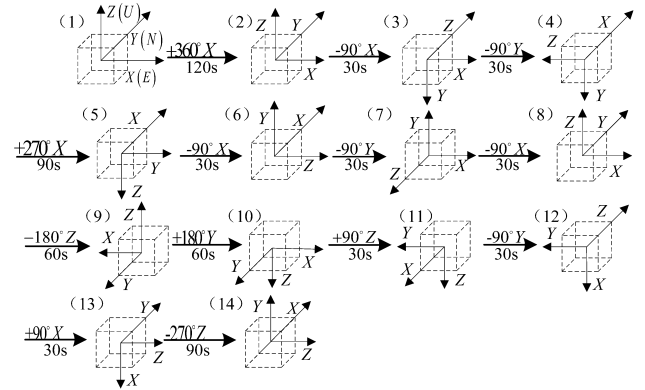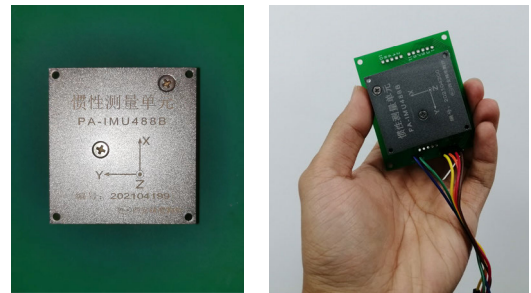
simulation data for path planning was generated, and the simulation parameters are shown in Table 3. Then, we used the method proposed in this study for path planning, and the target observability degree was selected as $\sigma_{max} = 10$, the maximum number of rotations is $r_{max} = 50$. The sensor sampling frequency was 400 Hz. The initial attitude errors were set as $\begin{bmatrix} 5' & 5' & 5' \end{bmatrix}$, rotation angular rate was selected as 30 °/s, observation noise at zero velocity was $V_{v3\times1} = \begin{bmatrix} 0.01 & 0.01 & 0.01 \end{bmatrix}^T$ m/s, and position observation noise was $V_{p3\times1} = \begin{bmatrix} 0.01 & 0.01 & 0.01 \end{bmatrix}^T$ m.

According to the above calibration conditions, the rotation scheme obtained using the optimal path planning algorithm proposed in this study is shown in Fig. 11. MEMS-IMU was calibrated using hand according to the rotation scheme in Fig. 12, and the IMU was stationary for 90 s at the beginning and final positions respectively. The raw data of angular rate output by gyroscope and specific force output by accelerometer are shown in Fig. 13.

As shown in Fig. 13, the sensor data contains more interference during the process of IMU rotation without a turntable. And the angular rate of rotation was not stable, thereby increasing the difficulty of the error term estimation. We estimated the error terms using the system-level calibrated Kalman model proposed in Section II. B, and the results are shown in Fig. 14-15.

As shown in Fig. 14, all error terms of gyro converged within 5 min. From 0 s to 90 s, B_{gx} and B_{gy} were effectively estimated and converged rapidly. At 90 s after the
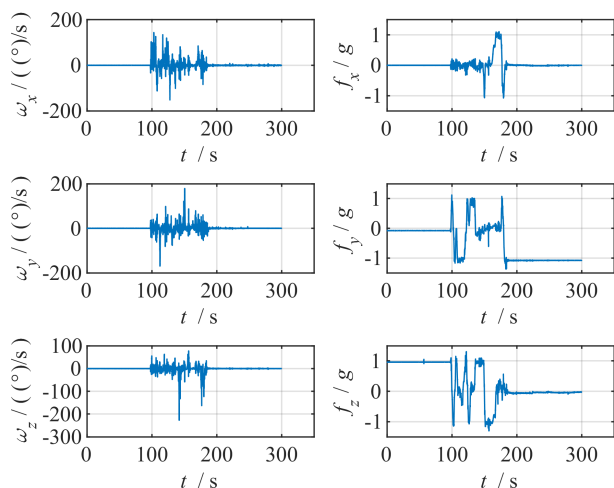
FIGURE 13. Output data of IMU.

FIGURE 14. System level calibration experiment results of (a) Gyro bias error, (b) Gyro scale factor error, (c) Gyro non-orthogonal error.

rotation began, it can be seen that all scaling factor errors and non-orthogonal errors were estimated, which was slightly different from the situation in the simulation. That was because the IMU rotation was performed manually, so the actual rotation was not strictly around the X, Y, or Z axis. In the process of rotation of a certain axis, other error terms were also motivated to some extent. In fact, this situation was not a good influence, which may reduce the decoupling effect of the calibrated path and create a gap with the expected results. During this time, B_{gz} fluctuated considerably, not converged. In the final stationary phase, B_{gz} gradually converged, and the other errors did not diverge.

Fig. 15 showed the system-level calibration experiment results of accelerometer. From 0 s to 90 s, B_{ax}, B_{ay} and B_{az} were effectively estimated and converged rapidly. At 90 s after the rotation began, it can be seen that B_{ax}, B_{ay} converges to another value. It was because the errors were coupled with each other before the rotation began, so that B_{ax}, B_{ay} were incorrectly estimated. After the optimal calibration path, each error term was decoupled, and B_{ax}, B_{ay} gradually converged to the correct value. The convergence characteristics of the other errors were similar to that of the gyroscope. Fig. 14-15 declared that the by the optimal calibration path, the estimated results of 21 error terms can converge under the current calibration experimental conditions within 5 min.

In order to verify the repeatability of the calibration path results, three repeated experiments were performed, and the calibration results were listed in Table 4. As shown in Table 4, the repeatability of the estimates of most of the error terms in the three experiments is favorable, indicating the effective-ness of the method proposed in this study. Although there were some differences between the calibration results and the preset error size during the calibration path planning, the experimental results can still converge stably. It showed that the relatively rough sensor error setting will not affect the convergence of the error estimation when the calibration
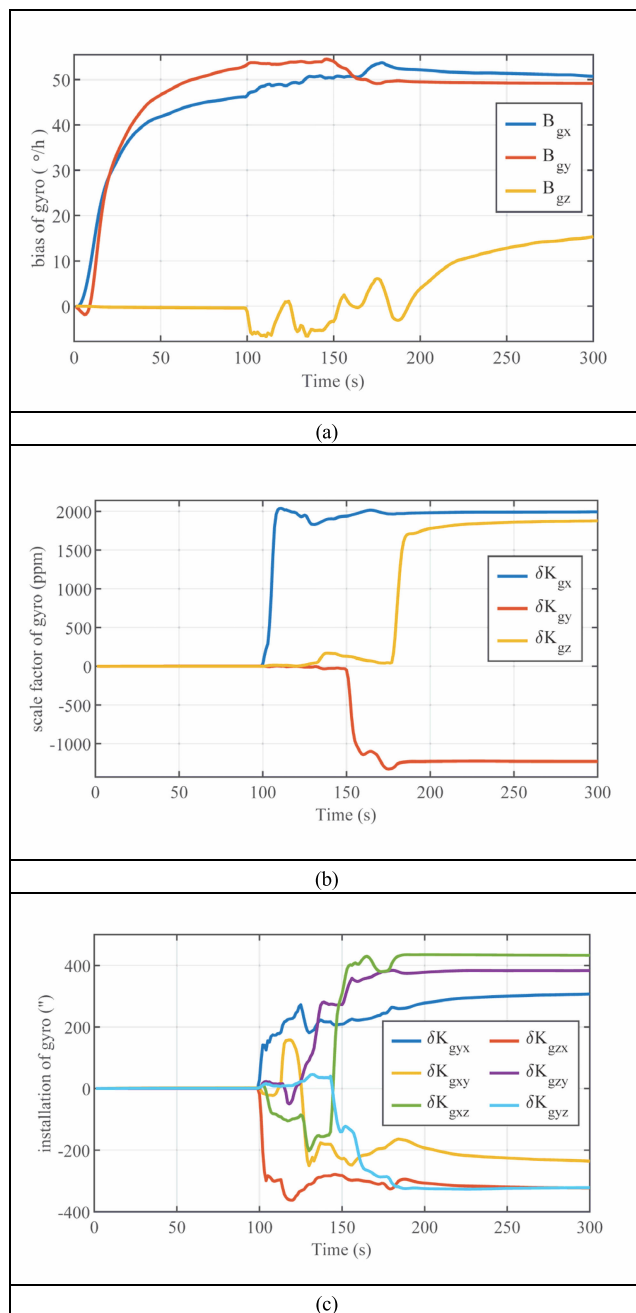
conditions were set. Moreover, the error of MEMS sensor will change every time it is powered on again, so it is normal that there are some differences between the results of fractional calibration and system-level calibration.

To evaluate the calibration results obtained by the proposed method of this study, the error terms of PA-IMU488B were also calibrated using a six-position discrete calibration method on a three-axis turntable, and each position required 5 min, for a total of 30 min. The compared results of two calibrations (six-position discrete calibration and system level
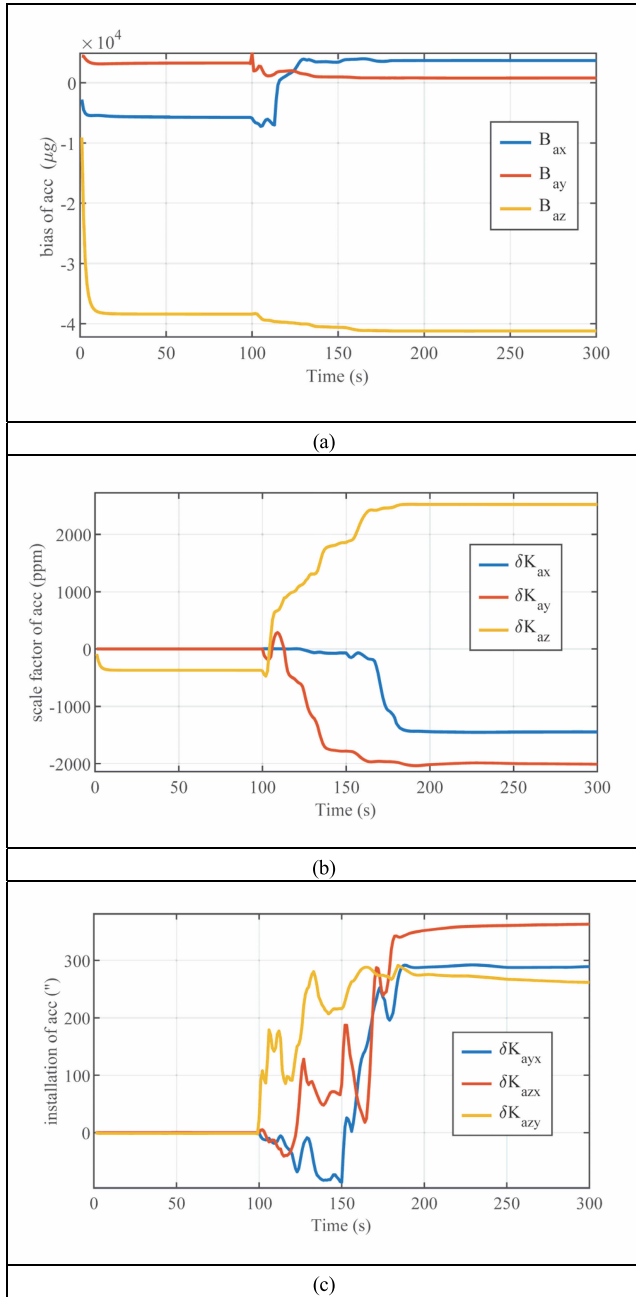
FIGURE 15. System level calibration experiment results of (a) Accelerometer bias error, (b) Accelerometer scale factor error, (c) Accelerometer non-orthogonal error.

TABLE 3. Path planning algorithm sensor error setting.

Error terms	Error values
gyro constant bias ($°/h$)	40
acc constant bias (mg)	2
angular random walk ($°/\sqrt{h}$)	0.25
velocity random walk ($\mu g/\sqrt{Hz}$)	100
gyro scale factor error (ppm)	2000
acc scale factor error (ppm)	2000
gyro non-orthogonal error ($''$)	500
acc non-orthogonal error ($''$)	500

TABLE 4. System level calibration experiment results.

Error coefficients	Systematic calibration			Average value
	1	2	3	
B_{gx} ($°/h$)	52.95	50.70	50.95	51.53
B_{gy} ($°/h$)	52.11	49.15	47.73	49.66
B_{gz} ($°/h$)	13.51	15.33	12.14	13.66
δK_{gx} (ppm)	1966.30	1993.97	1987.39	1982.55
δK_{gy} (ppm)	-1256.76	-1230.18	-1252.99	-1246.64
δK_{gz} (ppm)	1896.31	1878.21	1870.64	1881.72
δK_{gyx} ($''$)	316.40	307.30	304.06	309.25
δK_{gzx} ($''$)	-318.60	-323.28	-328.88	-323.59
δK_{gxy} ($''$)	-238.98	-235.41	-241.00	-238.46
δK_{gzy} ($''$)	378.41	383.05	385.63	382.46
δK_{gxz} ($''$)	430.38	432.90	436.59	433.29
δK_{gyz} ($''$)	-322.75	-321.91	-326.52	-323.73
B_{ax} (μg)	3626.83	3702.55	3753.79	3694.39
B_{ay} (μg)	780.39	799.66	801.36	793.80
B_{az} (μg)	-41220.2	-41210.6	-41217.4	-41216.07
δK_{ax} (ppm)	-1415.54	-1446.60	-1426.62	-1429.59
δK_{ay} (ppm)	-1973.08	-2010.11	-2026.49	-2003.23
δK_{az} (ppm)	2470.57	2521.05	2515.99	2502.54
δK_{ayx} ($''$)	270.90	289.24	266.55	275.56
δK_{azx} ($''$)	344.51	362.83	351.81	353.05
δK_{azy} ($''$)	276.77	261.76	284.50	274.34

TABLE 5. Comparison of system - level calibration results with discrete calibration results.

Error coefficients	Discrete calibration	Average value	Difference value
B_{gx} ($°/h$)	50.77	51.53	0.76
B_{gy} ($°/h$)	49.19	49.66	0.47
B_{gz} ($°/h$)	14.24	13.66	0.58
δK_{gx} (ppm)	1962.23	1982.55	20.32
δK_{gy} (ppm)	-1243.63	-1246.64	3.01
δK_{gz} (ppm)	1915.65	1881.72	33.93
B_{ax} (μg)	3634.49	3694.39	59.90
B_{ay} (μg)	792.68	793.80	1.12
B_{az} (μg)	-41321.90	-41216.07	105.83
δK_{ax} (ppm)	-1463.62	-1429.59	34.03
δK_{ay} (ppm)	-1943.87	-2003.23	59.36
δK_{az} (ppm)	2541.72	2502.54	39.18

calibration) are listed in Table 5. It can be seen from Table 5 that the results of system-level calibration are consistent with those of discrete calibration, indicating that the proposed method can correctly achieve system-level calibration of IMU sensors. Among them, the error parameter with the largest residual error was the Z-axis deviation of the accelerometer, which was mainly because its magnitude was too different from the expected value, which may lead to inadequate error estimation.

The total time required for the system-level calibration was 5 min, which was a sixth of the time spent for the discrete calibration. It was demonstrated that the method proposed in this study can be used to achieve accurate calibration of MEMS-IMU errors in a relatively short time without the use of a turntable.

V. DISCUSSION

A. CALIBRATION OF HIGH ACCURACY IMUS

For calibrating small batches of high accuracy IMUs, we predominantly focused on if the calibration path could be sufficiently motivated by the error term to obtain accurate calibration results; the calibration time was a secondary concern. We adopted the path planning method proposed in this study and improved the calibration accuracy for high precision IMUs by increasing the set observability degree target as well as the number of rotations to further improve the incentive effect of the error term.

B. FOR LARGE BATCH IMU CALIBRATION

For large batch IMU calibration, it is required to reduce the calibration time for sensor testing. The calibration path design using the method proposed in this study can effectively reduce the calibration time while ensuring calibration accuracy.

To further decrease the calibration time, the method proposed in this study can be first used to obtain a calibration path by roughly setting the simulation parameters, and then, a more accurate error estimation result can be obtained through a calibration test. The calibration results are then used to re-plan the path using the method proposed in this study to obtain the optimal calibration path for this batch of sensors. Through such an iterative approach, the limitation of non-optimal times due to excessive deviations of the simulation error terms set roughly in the application of this method can be solved.

C. IN-FIELD CALIBRATION WITHOUT A TURNTABLE

For in-field calibration without a turntable, the sensor errors must be adequately motivated because of the lack of accurate outside information. The insufficient motivation of sensor errors will result in the information of each error term being lost in the noise and not being accurately identified. According to the system-level calibration path planning method proposed in this study, it is possible to ensure that each error term is effectively motivated. Therefore, for serious noise interference, a reasonable calibration path planning can still achieve the recognition of the error terms, which is important for improving the IMU in-field calibration accuracy.

VI. CONCLUSION

In this study, a system-level calibration path planning method based on the improved Dijkstra algorithm was proposed. Based on the principles of observability degree analysis and system-level calibration, a system-level calibration path planning algorithm was designed, a 30-dimensional Kalman filtering model was established, and a system-level calibration scheme was proposed. Herein, each error of the sensor was fully motivated by improving the effectiveness of the calibration path. The results demonstrated that this method can construct the optimal calibration path for IMUs with different

calibration conditions and different accuracy levels as well as considerably reduce the calibration time and achieve the preset target accuracy. The feasibility of the method was verified via simulations and experiments. For the MEMS-IMU, the error reached the target accuracy within 5 min without using equipment, such as a turntable., providing a reliable calibration path for the in-field calibration of the MEMS-IMU under different conditions.

REFERENCES

[1] D. H. Titterton and J. L. Weston, *Strapdown Inertial Navigation Technology*, 2nd ed. London, U.K.: IET, 2004.

[2] T. Nieminen, J. Kangas, S. Suuriniemi, and L. Kettunen, "An enhanced multi-position calibration method for consumer-grade inertial measurement units applied and tested," *Meas. Sci. Technol.*, vol. 21, no. 10, Oct. 2010, Art. no. 105204, doi: 10.1088/0957-0233/21/10/105204.

[3] X. Ru, N. Gu, H. Shang, and H. Zhang, "MEMS inertial sensor calibration technology: Current status and future trends," *Micromachines*, vol. 13, no. 6, p. 879, May 2022, doi: 10.3390/mi13060879.

[4] Q. Ren, B. Wang, Z. Deng, and M. Fu, "A multi-position self-calibration method for dual-axis rotational inertial navigation system," *Sens. Actuators A, Phys.*, vol. 219, pp. 24–31, Nov. 2014, doi: 10.1016/j.sna.2014.08.011.

[5] Z. C. Zheng, S. L. Han, and K. F. Zheng, "An eight-position self-calibration method for a dual-axis rotational inertial navigation system," *Sens. Actuators A, Phys.*, vol. 232, pp. 39–48, Aug. 2015, doi: 10.1016/j.sna.2015.05.002.

[6] M. S. Grewal, V. D. Henderson, and R. S. Miyasako, "Application of Kalman filtering to the calibration and alignment of inertial navigation systems," *IEEE Trans. Autom. Control*, vol. 36, no. 1, pp. 3–13, Jan. 1991, doi: 10.1109/9.62283.

[7] S. Poddar, V. Kumar, and A. Kumar, "A comprehensive overview of inertial sensor calibration techniques," *J. Dyn. Syst., Meas., Control*, vol. 139, no. 1, Jan. 2017, Art. no. 011006, doi: 10.1115/1.4034419.

[8] H. Fan, Y. Xie, Z. Wang, and L. Wang, "A unified scheme for rotation modulation and self-calibration of dual-axis rotating SINS," *Meas. Sci. Technol.*, vol. 32, no. 11, pp. 1–11, 2021, doi: 10.1088/1361-6501/ac12ff.

[9] B. Xie, Y. Y. Qin, and Y. H. Wan, "Multi-position calibration method of laser gyro SINS," *J. Chin. Inertial Technol.*, vol. 19, no. 2, pp. 157–163, Apr. 2011, doi: 10.13695/j.cnki.12-1222/o3.2011.02.005.

[10] B. Li, J. Lu, W. Xiao, and T. Lin, "In-field fast calibration of FOG-based MWD IMU for horizontal drilling," *Meas. Sci. Technol.*, vol. 26, no. 3, Jan. 2015, Art. no. 035001, doi: 10.1088/0957-0233/26/3/035001.

[11] Z. H. Wang, X. H. Cheng, and J. B. Fu, "Optimized multi-position calibration method with nonlinear scale factor for inertial measurement units," *Sensor*, vol. 19, no. 16, pp. 3568–3586, Aug. 2019, doi: 10.3390/s19163568.

[12] W. T. Fong, O. K. Ong, and A. Y. C. Nee, "Methods for in-field user calibration of an inertial measurement unit without external equipment," *Meas. Sci. Technol.*, vol. 19, no. 8, pp. 1–11, Jul. 2008, doi: 10.1088/0957-0233/19/8/085202.

[13] J. Lu, C. Lei, S. Liang, and Y. Yang, "An all-parameter system-level calibration for stellar-inertial navigation system on ground," *IEEE Trans. Instrum. Meas.*, vol. 66, no. 8, pp. 2065–2073, Aug. 2017.

[14] E. P. Mark, "Calibration and attitude determination with redundant inertial measurement units," *J. Guid., Control, Dyn.*, vol. 28, no. 4, pp. 743–749, Jul./Aug. 2005, doi: 10.2514/1.7040.

[15] L. Zhao, D. Guan, J. Rene, J. Cheng, and S. Kostyantyn, "An accurate and fault-tolerant target positioning system for buildings using laser rangefinders and low-cost MEMS-based MARG Sensors," *Sensors*, vol. 15, no. 10, pp. 27060–27086, Oct. 2015, doi: 10.3390/s151027060.

[16] Z. Wang, Y. Xie, X. Yu, H. Fan, G. Wei, L. Wang, Z. Fan, G. Wang, and H. Luo, "A system-level calibration method including temperature-related error coefficients for a strapdown inertial navigation system," *Meas. Sci. Technol.*, vol. 32, no. 11, Nov. 2021, Art. no. 115117, doi: 10.1088/1361-6501/ac0acd.

[17] B. Wang, Q. Ren, Z. Deng, and M. Fu, "A self-calibration method for nonorthogonal angles between gimbals of rotational inertial navigation system," *IEEE Trans. Ind. Electron.*, vol. 62, no. 4, pp. 2353–2362, Apr. 2015, doi: 10.1109/TIE.2014.2361671.

[18] M. Glueck, D. Oshinubi, P. Schopp, and Y. Manoli, "Real-time autocalibration of MEMS accelerometers," *IEEE Trans. Instrum. Meas.*, vol. 63, no. 1, pp. 96–105, Jan. 2014, doi: 10.1109/TIM.2013.2275240.

[19] J. Cheng, P. Liu, P. Gao, M. Zou, and W. Fu, "High-precision calibration scheme for RIMU," *IEEE Access*, vol. 7, pp. 72376–72386, 2019, doi: 10.1109/ACCESS.2019.2919587.

[20] B. Xu, L. Wang, and T. Duan, "A novel hybrid calibration method for FOG-based IMU," *Measurement*, vol. 147, Dec. 2019, Art. no. 106900, doi: 10.1016/j.measurement.2019.106900.

[21] L. Camberlein and F. Mazzanti, "Calibration technique for laser gyro strapdown inertial navigation system," in *Proc. Symp. Gyro Technol.*, Stuttgart, West Germany, 1985, p. 5.

[22] P. Wang, B. Lu, P. Yang, and F. Chen, "Systematic calibration method based on acceleration and angular rate measurements for fiber-optic gyro SINS," *Rev. Sci. Instrum.*, vol. 92, no. 1, Jan. 2021, Art. no. 015001, doi: 10.1063/5.0023674.

[23] L. Wang, Y. Hu, T. Wang, and B. Liu, "Vibration error correction for the FOGs-based measurement in a drilling system using an extended Kalman filter," *Appl. Sci.*, vol. 11, no. 14, p. 6514, Jul. 2021, doi: 10.3390/app11146514.

[24] Q. Z. Cai, G. L. Yang, N. F. Song, and Y. L. Liu, "Systematic calibration for ultra-high accuracy inertial measurement units," *Sensors*, vol. 16, no. 6, pp. 940–956, Jun. 2016, doi: 10.3390/s16060940.

[25] E. W. Dijkstra, "A note on two problems in connexion with graphs," *Numer. Math.*, vol. 1, no. 1, pp. 269–271, Dec. 1959.

[26] S. Alshammrei, S. Boubaker, and L. Kolsi, "Improved Dijkstra algorithm for mobile robot path planning and obstacle avoidance," *Comput., Mater. Continua*, vol. 72, no. 3, pp. 5939–5954, 2022.

[27] M. Luo, X. Hou, and J. Yang, "Surface optimal path planning using an extended Dijkstra algorithm," *IEEE Access*, vol. 8, pp. 147827–147838, 2020, doi: 10.1109/ACCESS.2020.3015976.

[28] K. Wei, Y. Gao, W. Zhang, and S. Lin, "A modified Dijkstra's algorithm for solving the problem of finding the maximum load path," in *Proc. IEEE 2nd Int. Conf. Inf. Comput. Technol. (ICICT)*, Mar. 2019, pp. 10–13, doi: 10.1109/INFOCT.2019.8711024.

[29] A. H. M. Santos, R. M. De Lima, C. R. S. Pereira, R. Osis, G. O. S. Medeiros, A. R. De Queiroz, B. K. Flauzino, A. R. P. C. Cardoso, L. C. Junior, R. A. Dos Santos, and E. L. C. Junior, "Optimizing routing and tower spotting of electricity transmission lines: An integration of geographical data and engineering aspects into decision-making," *Electr. Power Syst. Res.*, vol. 176, pp. 1–12, Jul. 2019.

[30] D.-D. Zhu and J.-Q. Sun, "A new algorithm based on Dijkstra for vehicle path planning considering intersection attribute," *IEEE Access*, vol. 9, pp. 19761–19775, 2021, doi: 10.1109/ACCESS.2021.3053169.

[31] F. M. Ham and R. G. Brown, "Observability, eigenvalues, and Kalman filtering," *IEEE Trans. Aerosp. Electron. Syst.*, vol. AES-19, no. 2, pp. 269–273, Mar. 1983, doi: 10.1109/TAES.1983.309446.

[32] J. Lu, L. Ye, J. Zhang, W. Luo, and H. Liu, "A new calibration method of MEMS IMU plus FOG IMU," *IEEE Sensors J.*, vol. 22, no. 9, pp. 8728–8737, May 2022, doi: 10.1109/JSEN.2022.3160692.

[33] M. Niu, H. Ma, X. Sun, T. Huang, and K. Song, "A new self-calibration and compensation method for installation errors of uniaxial rotation module inertial navigation system," *Sensors*, vol. 22, no. 10, p. 3812, May 2022, doi: 10.3390/s22103812.

[34] R. E. Kalman, "A new approach to linear filtering and prediction problems," *J. Fluids Eng.*, vol. 82, no. 1, pp. 35–45, Mar. 1960, doi: 10.1115/1.3662552.

[35] G. M. Yan, "Research on vehicle autonomous positioning and orientation system," Ph.D. dissertation, School Automat., Northwestern Polytech. Univ., Xi'an, China.

[36] S. Han, Z. Meng, O. Omisore, T. Akinyemi, and Y. Yan, "Random error reduction algorithms for MEMS inertial sensor accuracy improvement—A review," *Micromachines*, vol. 11, no. 11, p. 1021, Nov. 2020, doi: 10.3390/mi11111021.

XUESONG BAI received the B.S. degree in mechanical design manufacture and automation from the Harbin Institute of Technology, Weihai, Shandong, China, in 2020. His research interests include SINS and IMU calibration.

LU WANG received the B.S. degree in measurement and control technology and instrumentation from Henan University, Kaifeng, Henan, China, in 2011, and the Ph.D. degree in optical engineering from the Beijing University of Aeronautics and Astronautics, Beijing, China, in 2018.

She is currently with the Key Laboratory on Deep Geo-Drilling Technology, Ministry of Land and Resources, China University of Geosciences. Her research interest includes well-trajectory survey based on the inertial navigation technology.

YUANBIAO HU received the B.S., M.S., and Ph.D. degrees in geological engineering from the China University of Geosciences, Beijing, China, in 1999, 2002, and 2005, respectively.

He is currently a Professor with the China University of Geosciences. His research interests include geological drilling computer automation control technology and high-precision directional drilling technology.

PINGFEI LI received the B.S. degree in geological engineering from the China University of Geosciences, Beijing, China, in 2016. Her research interests include SINS and trenchless technology.

YUTONG ZU received the B.S. degree in geological engineering from the China University of Geosciences, Beijing, China, in 2016. Her research interests include SINS and trenchless technology.

• • •